https://doi.org/10.26599/FRICT.2025.9441210

Research Article

Steady shear rheological response of ferrofluids containing hydrophilic fumed silica under magnetic fields

Qianping Li[1], Decai Li [2,*], Yijian Wei[1], Shiting Zhang[1], Yang Hu[1], Jingcheng Cai[1], Sijia Liu[1], Lifen Liu[1], Zhibin Wang[1], Yajing Qiao[1]

[1]School of Mechanical, Electronic and Control Engineering, Beijing Jiaotong University, Beijing 100044, China

[2]State Key Laboratory of Tribology, Tsinghua University, Beijing 100084, China

[*]Electronic addresses for correspondence: lidecai@mail.tsinghua.edu.cn

Received: July 4, 2025; Revised: November 24, 2025; Accepted: December 26, 2025
© The Author(s) 2025.

Abstract:

This study investigates the steady shear rheological behavior of water-based ferrofluids composited with hydrophilic fumed silica under different magnetic field strengths, with particular attention to avoiding gelation that reduces fluidity. Seven composite ferrofluid samples were prepared and characterized. By adjusting silica particle size and volume fraction, their effects on viscosity and yield stress were explored. As a result, pronounced shear-thinning behavior is observed in this dispersion, with their flow curves under different magnetic field strengths effectively scaled by the Mason number. Higher silica concentration or larger particle size increases the critical Mason number, showing that field-induced structures become more stable. In contrast, only high silica concentrations significantly enhance shear-thinning, as reflected by a larger flow index, whereas particle size has little influence. Yield stress analysis further shows that macroscopic models capture normalized Bingham yield stress, while microscopic models better predict normalized static yield stress. Overall, this work demonstrates that hydrophilic fumed silica offers a simple and effective route to tune the magnetorheology of water-based ferrofluids without inducing gelation, ensuring controllable rheology and good fluidity.

1. Introduction

Ferrofluids (magnetic fluids) are colloidal suspensions consisting of ferromagnetic or ferrimagnetic nanoparticles such as γ-Fe_2O_3 or Fe_3O_4, with particle sizes typically ranging from 5 to 15 nanometers. To achieve stable dispersion and prevent particle aggregation and sedimentation, magnetic nanoparticles are often surface-modified through mechanisms such as electrostatic

Just Accepted

repulsion or steric hindrance, effectively counteracting van der Waals forces and magnetic dipole interactions[1,2]. ferrofluids exhibit both the fluidity of liquids and the magnetic responsiveness of solids. This dual characteristic enables their wide application prospects in fields such as optics[3–5], mechanics[6,7], thermal systems[8,9], and biomedicine[10–12]. Over the years, ferrofluids have evolved into reliable functional materials for addressing complex engineering challenges and have found practical applications in various fields, including vacuum sealing in spacecraft[13,14], contactless lubrication in aircraft engines[14], vibration damping in weapon systems[15,16], targeted drug delivery[17] and MRI contrast enhancement in biomedical applications[11,18].

Moreover, ferrofluid has also been an ideal soft material for probing transitions from solid-like to liquid-like behavior. Under an external magnetic field, the spatial distribution and alignment of nanoparticles are reconfigured, thereby significantly altering macroscopic rheological properties such as viscosity, yield stress, and viscoelasticity[19][20]. Studies have shown that the magnetorheological response of magnetic fluids can be effectively tuned by adjusting factors such as nanoparticle volume fraction, morphology, concentration, magnetic field strengtsh, and types of additives[21–24]. Recently, Sun et al. systematically reviewed the preparation strategies, physicochemical properties, and tribological performance of magnetic lubricants under magnetic fields, highlighting their potential in advanced lubrication and heat transfer system[25]. Many practical applications impose specific requirements on the tunable rheological properties of ferrofluids—for instance, magnetorheological dampers require fast response and high yield stress[26]; magnetic seals and lubrication systems demand low viscosity and long-term stability[27]; recent tribological studies show that external magnetic fields tune ferrofluid viscosity and yield stress, thereby modifying their lubrication regime and frictional response[28]. and microfluidic devices necessitate precise control over shear behavior and hysteresis[29]. Therefore, a comprehensive understanding of key parameters—such as viscosity, yield stress, and hysteresis—is crucial for the effective design and application of ferrofluids.

Recent studies have shown that the incorporation of functional additives can significantly improve the rheological properties of magnetic fluids. In contrast to solely tuning magnetic field strength or particle concentration, incorporating additives enables more versatile and targeted control of rheological behavior. For example, multi-walled carbon nanotubes can inhibit the formation of magnetic microstructures, leading to reduced viscosity and yield stress, while simultaneously enhancing the thermal conductivity of the system[30]; In magnetorheological fluids, adding inorganic nanoparticles has been shown to simultaneously tune viscosity, damping capacity, and thermal behavior in practical devices, such as MR dampers used in hard turning[31]; biological nanotubes can significantly enhance magnetoviscous effects and improve overall rheological performance[32]; and silica nanoparticles can form network structures that modulate shear-thinning behavior and viscoelasticity. In particular, inverse ferrofluids—composite systems containing micrometer-scale silica particles suspended in a continuous magnetic medium—exhibit enhanced magnetorheological performance. Early work by Skjeltorp revealed the formation of linear particle chains under magnetic fields[33], and subsequent studies established that viscosity, yield stress, and structural response in such systems strongly depend on Mason number, particle fraction, and field strength[34,35,21][36].Among these additives, hydrophilic fumed silica is of particular interest due to its solvent-dependent interaction behavior. In nonpolar medium, where the solvent cannot form hydrogen bonds with the surface silanol groups (Si–OH) of the silica particles, hydrogen bonding between adjacent silica particles promotes the formation of a three-dimensional network, resulting

Just Accepted

in gel-like behavior[37]. In contrast, in polar media such as water, hydrogen bonding between solvent molecules and the silica surface produces a solvation layer that generates short-range non-DLVO (Derjaguin–Landau–Verwey–Overbeek) repulsive forces, preventing direct particle–particle contact and maintaining stable dispersion[37] [38]. This dual behavior highlights the critical role of solvent properties in determining whether hydrophilic silica induces gelation or stabilizes dispersion.

Despite the growing interest in silica-modified ferrofluids, systematic studies on the interaction mechanisms of hydrophilic fumed silica in polar (water-based) ferrofluids remain scarce. Existing reports have focused mainly on oil-based systems[39,40]. J. de Vicente et al. [41] showed that moderate silica addition improves stability but excessive amounts hinder magnetic structure formation. S. Alves et al. [42] found that hydrophilic silica enhanced viscosity and shear stress under low magnetic fields, but resulted in weaker thixotropic recovery and lower yield stress compared with hydrophobic silica. J. Felicia et al.[43] demonstrated that hydrophilic silica disrupts dipolar interactions, thereby reducing viscoelasticity and suppressing chain formation. However, these effects have been investigated almost exclusively in oil-based ferrofluids, while how fumed silica–water hydrogen bonding affects field-induced structures in water-based ferrofluids remains unexplored. Water-based systems are low-toxic, environmentally safe, and biocompatible[44–46]. Therefore, studying the role of hydrophilic fumed silica in water-based ferrofluids is important for both fundamental study and future applications.

Building on this gap, we study water-based ferrofluids with hydrophilic fumed silica and show how silica changes viscosity, yield stress, and flow behavior under magnetic fields without causing gelation. Unlike oil-based systems, the water–silica hydrogen bonding and solvation create different dispersion stability and field-induced structures. We further show that macroscopic energy-scaling models describe the normalized dynamic yield stress, while microscopic chain models are better suited for the normalized static yield stress, thereby revealing the mechanisms of field-induced rheological behavior. In practice, adding a small amount of silica provides a simple and effective way to tune rheology while keeping good processability and pumpability, which is important for cooling, sealing and pumping, damping, and microfluidic applications.

2. Materials and Methods

In this study, a commercial water-based ferrofluid with an average magnetic nanoparticle size of approximately 10 nm was used as the magnetic base fluid and its basic properties are summarized in Table 1. Hydrophilic fumed silica nanoparticles (purchased from Aladdin) with specific surface areas of 395 ± 25 m²/g (denoted as S7, average particle size ~7 nm) and 195 ± 15 m²/g (S14, ~14 nm) were used. silica nanoparticles of two different sizes and volume fractions (1.1 vol%, 1.7 vol%, and 2.8 vol%) were dispersed into the ferrofluid to prepare seven composite ferrofluid suspensions with varying formulations. The dispersions were homogenized using an ultrasonic cleaner (JP-031PLUS, 6.5 L capacity, 40 kHz) operated at 60 °C with an ultrasonic output power of 200 W for 20 min to ensure a uniform distribution of silica nanoparticles. The characteristics of hydrophilic fumed silica dispersed in water-based ferrofluids are summarized in Table 2. These samples were systematically characterized, and the results are discussed in Section 3.

Table 1. Physical properties of the water-based ferrofluid.

Just Accepted

Sample	Volume fraction of magnetic nanoparticles	Density(kg/m^3)	Saturation magnetization (kA/m)	Viscosity η_c(mPa s)
water-based ferrofluid	0.0637	1.18	13.519	3.9

The steady shear magnetorheological behavior was measured using an Anton Paar MCR 302 magnetorheometer in a parallel-plate configuration with a fixed gap of 84 μm. This gap was chosen to reduce wall slip and keep the magnetic field uniform. Our preliminary tests showed that larger gaps (≥200 μm) led to unstable torque signals, while very small gaps (<80 μm) not only caused unreliable filling of the measurement volume but also generated excessive normal forces along the rotor axis, which made the experiments impossible to carry out. These observations are consistent with the findings of Yoshimura and Prud'homme[47], who reported that viscosity can change with gap size when wall slip occurs. In addition, a relatively small gap helps preserve the uniformity of the applied magnetic field and minimize radial field gradients within the parallel-plate geometry, which is essential for obtaining reliable magnetorheological responses, which is essential for obtaining reliable magnetorheological responses[48–50]. Therefore, 84 μm was used as a suitable gap for stable and accurate measurements.

An external magnetic field of up to 401 kA/m was applied using an electromagnet, oriented perpendicular to both the parallel plates and the shear direction. The diameter of the plates was 20 mm, and the temperature was maintained at 20 °C during the tests. Although the shear rate is not constant in this geometry, the parallel-plate configuration was preferred over the cone–plate geometry because the field-induced microstructure in magnetorheological fluids is highly dependent on the confining geometry[34,51], and the structure can be conveniently modulated by adjusting the plate gap.

Table 2. Characteristics of hydrophilic fumed silica dispersed in water-based ferrofluids.

Sample	Average particle size (nm)	Specific surface area (m²/g)	Volume fraction of silica in ferrofluid (%)
S14_1.1%	13.64	195 ± 15	1.1
S14_1.7%	13.64	195 ± 15	1.7
S14_2.8%	13.64	195 ± 15	2.8
S7_1.1%	6.82	395±25	1.1
S7_1.7%	6.82	395±25	1.7
S7_2.8%	6.82	395±25	2.8

The experimental procedure was as follows: (i) pre-shear the sample at a constant shear rate of 500 s^{-1} for 50 s; (ii) stop the shear and allow the suspension to equilibrate for 1 minute; (iii) increase the shear rate logarithmically from 0.1 to 8000 s^{-1}. If a magnetic field was to be applied, it was maintained during both steps (ii) and (iii). The apparent viscosity was calculated from the measured shear stress (taken at the two-thirds of the plate) divided by the corresponding shear rate. Under an applied magnetic field, composite ferrofluids containing fumed silica typically exhibited Bingham fluid behavior. Thus, the "true" yield stress was determined by multiplying the yield stress output from the software by ¾, following the method of Brunn and Asoud[52]. Additionally, sufficiently long acquisition times were maintained at each shear stress point to ensure steady-state

Just Accepted

measurements, especially for low-shear viscosity determination. For example, in a composite ferrofluid sample containing 1.1 vol% S7 silica, the variation in low-shear viscosity remained within 10% when the acquisition time per data point was changed from 10 s to 50 s. All measurements were repeated at least three times using freshly prepared samples, and the results are reported as mean values with standard deviations. All measurements were repeated at least three times using freshly prepared samples, and the results are reported as mean values with standard deviations. Error bars are not displayed in the figures because the uncertainties are consistently very small (typically <3%) and fall within the symbol size.

3. Results and Discussion

3.1 Characterization of Samples

The microstructures of the ferrofluids before and after the addition of hydrophilic fumed silica were observed using a scanning electron microscopy (SEM) (Gemini 300, Germany). As shown in Fig.1, image (a) presents the SEM image of the magnetic nanoparticles in the pure water-based ferrofluid, where the particles are relatively uniformly dispersed. Image (b) shows the composite ferrofluid containing hydrophilic fumed silica, which exhibits a noticeably rougher surface and more densely packed particles.

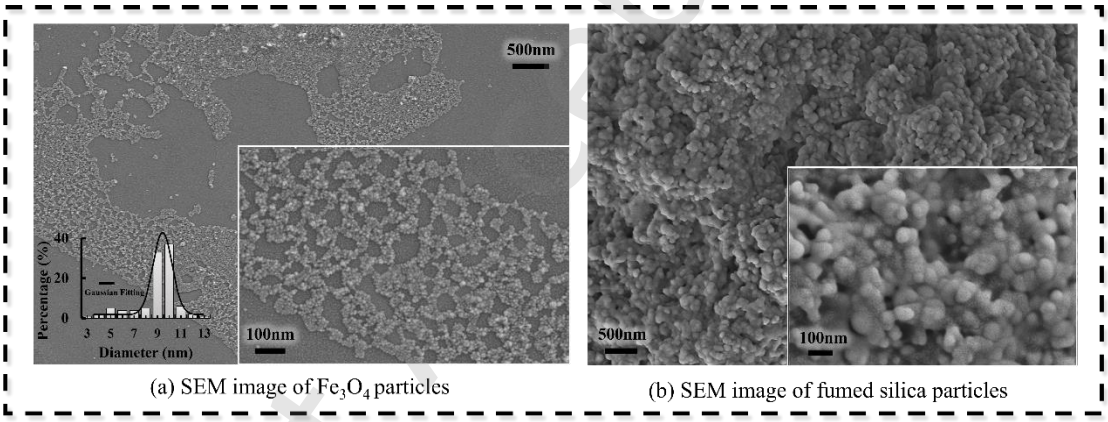

(a) SEM image of Fe_3O_4 particles (b) SEM image of fumed silica particles

Fig.1 Micrographs using scanning electron microscope with the inset showing an enlarged view of the local region.

The magnetic properties of all samples were measured at room temperature using an EZ9 vibrating sample magnetometer (VSM). The initial magnetization curves were obtained under an applied magnetic field ranging from 0 to 1500 kA/m, followed by sweeping the field from +1500 kA/m to -1500 kA/m and back to +1500 kA/m to generate complete hysteresis loops, as shown in Fig.2, all samples exhibit superparamagnetic behavior with typical sigmoidal Langevin-type curves. According to the Langevin function[53,54]:

$$M = M_s - \chi_h \cdot \frac{1}{H} \tag{1}$$

where M_s is the saturation magnetization of the water-based ferrofluid and χ_h is the high-field susceptibility. To obtain the saturation magnetization， we plotted the magnetization versus the inverse of the applied field $1/H$ and carried out a linear fit to the portion of the curve next to the *y*-axis, which corresponds to small $1/H$ (large external fields). The point where the linear fit crossed the *y*-axis was taken as the saturation magnetization as shown in the inset of Fig.2(a). The results show that the saturation magnetization of all composite ferrofluids containing hydrophilic

Just Accepted

fumed silica is very close to that of the unmodified aqueous ferrofluid, with values around 13.519 ± 0.5 kA/m (approximately 169.89 Gs), indicating that the fumed silica, as a non-magnetic component, contributes negligibly to the magnetic response. The magnetism mainly originates from the magnetic nanoparticles in the magnetic base fluid. According to the equation $M_s = \phi M_p$[53,54], where M_p is the saturation magnetization of the magnetic nanoparticles (209.44 kA/m in this case), the particle volume fraction ϕ is approximately 6.37%. In addition, the ferrofluid permeability data required for calculating the contrast factor β and the Mason number were obtained from the magnetization measurements as shown in the inset of Fig.2(b), the detailed parameters are listed in Table 3.

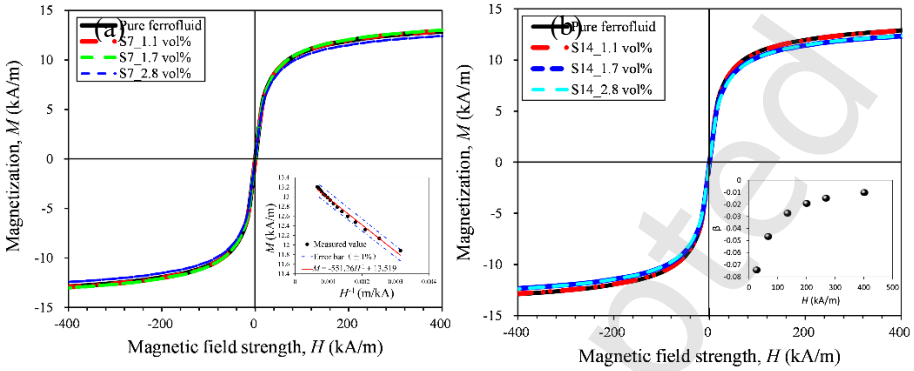

Fig.2 Hysteresis curves for pure ferrofluid and composite ferrofluids containing hydrophilic fumed silica. The inset shows *M*-1/*H* plot used to determine saturation magnetization (a) and the field dependence of the contrast factor in the pure ferrofluids (b).

Table 3. Magnetic permeability of the water-based ferrofluids at different magnetic field strengths from (Fig.2) and contrast factor according to $\beta = (1 - \mu_{cr})/(1 + 2\mu_{cr})$.

H_0 (kA/m)	**Pure ferrofluid permeability (μ_{cr})**	**Contrast factor (β)**
27	1.262	-0.074
67	1.154	-0.047
134	1.086	-0.027
201	1.060	-0.019
267	1.045	-0.015
401	1.031	-0.010

The presence of fumed silica in the composite ferrofluids was confirmed by energy-dispersive spectroscopy (EDS). As shown in Fig. 3(a), the spectrum of the pure ferrofluid reveals Fe and O as the main elements, while the Si content is only 2.52%, which is likely due to trace contamination from the glass container during sample preparation. In contrast, Fig. 3(b) shows that the Si content increases markedly to 12.44% in the sample containing 1.1 vol% S7, confirming the successful introduction of fumed silica into the ferrofluid.

Furthermore, as shown in Fig.4, the addition of fumed silica leads to a red-shift (i.e., a shift to lower wavenumbers) and broadening of the O–H stretching band (~3360 cm^{-1}), The H_2O bending vibration (~1650 cm^{-1}) also changes, which indicates that stronger hydrogen bonding between water molecules and surface silanol groups. In addition, the stronger Si–O–Si absorption at ~1080 cm^{-1} confirms the presence of silica in the system. These results agree with previous ATR-FTIR studies

Just Accepted

on colloidal silica[55], which showed that silica forms strongly hydrogen-bonded water layers at low concentrations. Notably, compared with S7 at the same volume fraction, S14 exhibits a more pronounced red-shift and broadening of the O–H band, a stronger H_2O bending band, and an intensified Si–O–Si absorption, indicating stronger interfacial hydrogen bonding and more developed solvation layers around larger silica particles. Together, these findings reveals that hydrogen bonding drives the formation of solvation layers on silica particles, which keep them well dispersed in water and thereby enhance the overall stability of the water-based ferrofluids.

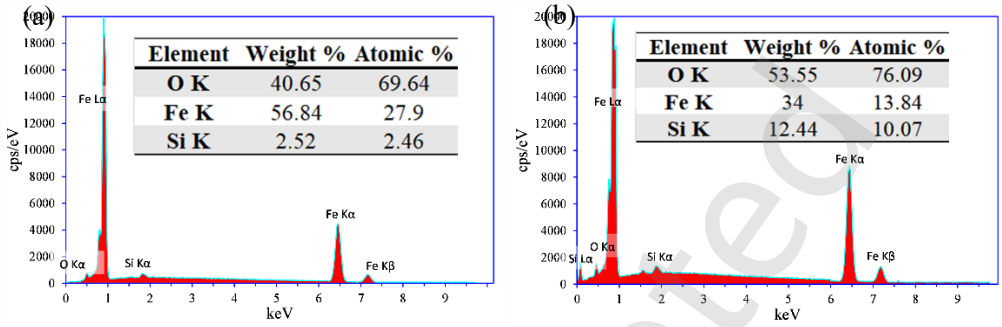

Fig.3 EDS spectra of (a) pure ferrofluid; (b) composite ferrofluids containing hydrophilic fumed silica (S7_1.1 vol%).

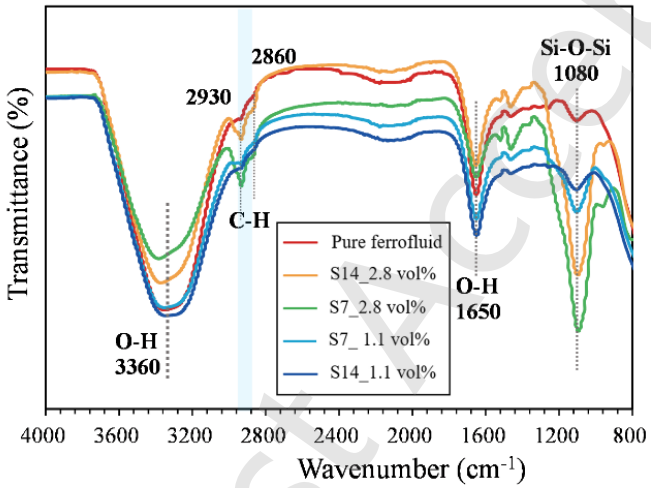

Fig.4 FT-IR spectra of pure ferrofluid and composite ferrofluids containing hydrophilic fumed silica with different particle sizes and volume fractions.

The water-based ferrofluid was used as the magnetic base fluid in this case. and its rheological behavior with and without magnetic fields is shown in Fig. 5. The results indicate that the ferrofluid exhibits nearly Newtonian behavior in the absence of a magnetic field. Under a magnetic field of 134 kA/m, the pure ferrofluid develops a yield stress and displays characteristics of a Bingham fluid. The solid lines represent the Bingham model fits, which agree well with the experimental data, and he two flow curves (with and without magnetic field) are nearly parallel, indicating that the plastic viscosity η_c remains essentially unchanged at approximately 3.9 mPa·s.

Just Accepted

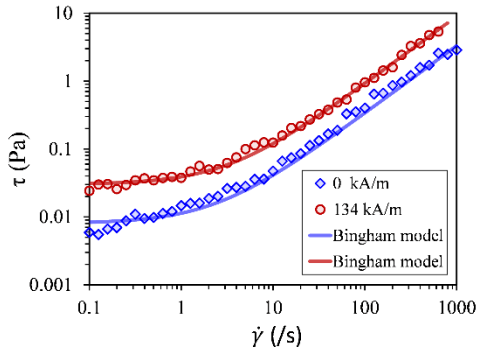

Fig.5 Flow curves of the pure ferrofluid under magnetic fields of 0 kA/m and 134 kA/m; the bule solid lines and red solid lines represent linear fits based on the Bingham model.

Notably, In this study, the volume fraction of hydrophilic fumed silica was kept below 2.8 vol% to avoid gelation and ensure stable dispersion. As noted in the introduction, fumed silica forms hydrogen bonds with water, which improves colloidal stability but can also cause gelation at higher concentrations. Here, small amounts of silica are used as a simple additive to adjust the rheological properties of ferrofluids, while avoiding gelation to keep good fluidity, fast response, and stable performance in applications.

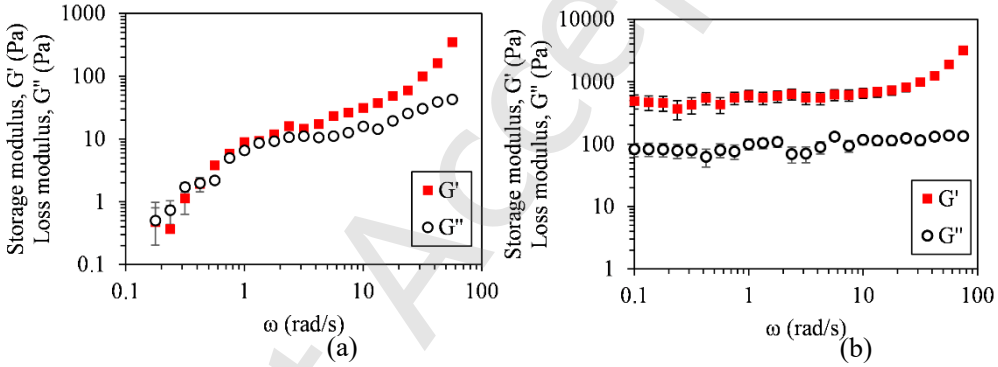

Fig.6 Small-amplitude oscillatory shear (SAOS) responses of the composite ferrofluid samples: (a) 2.8 vol% and (b) 3.78 vol%. The storage modulus G′(red squares) and loss modulus G″(open circles) are plotted as functions of angular frequency ω.

To verify this mechanistic consideration, additional samples with 3.8 vol% silica were prepared and tested using small-amplitude oscillatory shear (SAOS), which is widely used to probe the viscoelastic properties of complex fluids and to distinguish between sol-like and gel-like states[56–58]. Prior to frequency sweeps, strain-amplitude tests confirmed that the selected amplitude of 0.5% was within the linear viscoelastic regime (LVR). Fig.6 shows the frequency responses of dispersions with (a) 2.8 vol% and (b) 3.8 vol% fumed silica. For the 2.8 vol% sample, both G′ and G″ increase markedly with frequency without approaching frequency-independent plateaus. The corresponding loss tangent (tan δ=G″/G′) is above unity at low frequencies, decreases below unity at higher frequencies, and varies continuously across the range. No Winter–Chambon critical gel behavior (i.e., tan δ remaining constant across the frequency range) [56,57] is observed. indicating a sol-like, liquid-dominated state without gelation. In contrast, the 3.8 vol% sample exhibits G′≫ G″ throughout the frequency, with tan δ<1 and nearly frequency-independent behavior, which is

Just Accepted

characteristic of a percolated gel network[59,60]. These results confirm that gelation occurs at 3.8 vol%, while the 2.8 vol% sample remains ungelled.

3.2 Flow curve: Mason number scaling

Figure 7 shows the shear viscosity of the composite ferrofluid containing 2.8 vol% S7 fumed silica under varying magnetic field strengths. The results indicate that the system exhibits pronounced shear-thinning behavior across all field conditions and the viscosity increases significantly as the magnetic field strength rises. This suggests that magnetically induced alignment of particles into chain-like or columnar structures increases the fluid's resistance to flow. However, when the magnetic field exceeds 133 kA/m, the increase in viscosity becomes less pronounced, indicating that the system approaches magnetic saturation—where the magnetic nanoparticles have already formed well-developed structures with limited potential for further enhancement. At high shear rates, the viscosity curves tend to level off at a constant value, independent of the magnetic field strength, which is solely depends on the particle volume fraction and the dispersing medium viscosity.

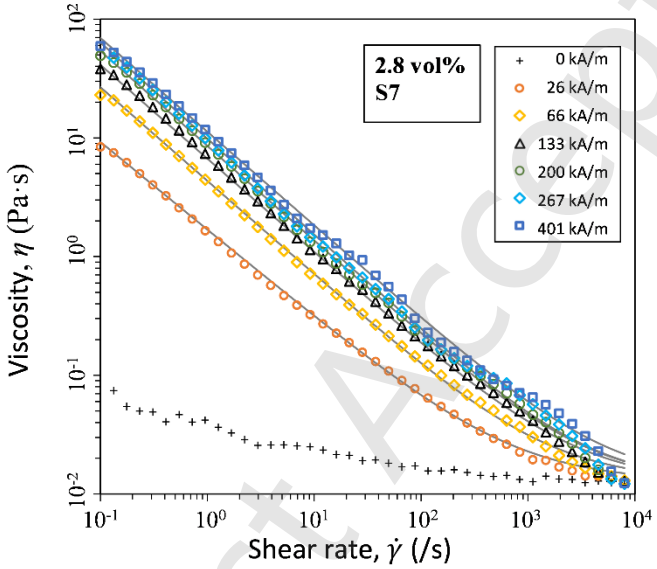

Fig.7 Typical shear viscosity curves of the composite ferrofluid containing 2.8 vol% S7 fumed silica under different magnetic field strengths, where the solid lines correspond to the fitting results calculated from Equation (2).

Data shown in Fig.7 follow a power law behavior. Solid lines included in Fig.7 correspond to the following fitting formula[61]:

$$\eta = c\dot{\gamma}^{-n} + \eta_{\infty}, \tag{2}$$

where c and η_{∞} are fitting constants and the high-shear viscosity, n is the flow index, which characterizes the system's response to shear rate and reflects the stability of the field-induced microstructures, with higher values implying stronger resistance to shear-induced deformation. In different ferrofluid systems, the strength, length, flexibility, and fracture threshold of chain-like or columnar structures can vary significantly. These structures form and disintegrate dynamically under shear, leading to variations in the observed flow index. Generally, a value of $n = 1$ indicates Newtonian behavior, $n < 1$ corresponds to shear-thinning fluids, and $n > 1$ is typical of shear-thickening fluids.

Just Accepted

As shown in Table 4, the fitted flow index n remains consistently around 0.8 across different magnetic field strengths. This indicates that the composite ferrofluid in this case exhibit pronounced shear-thinning behavior under the test conditions. The result is consistent with previous studies, where flow indices ranging from 0.74 to 0.9 have been reported for ferrofluids containing various types of silica particles[61–63]. It is worth noting that the observed n values are significantly lower than the ideal prediction of $n = 1$ from chain-based micromechanical models[64], but slightly higher than the theoretical value of $n = 2/3$ derived by Halsey et al[65], which was based on rigid ellipsoidal aggregates. This suggests that the magnetic nanoparticles in the present system form flexible, field-induced structures that can partially break down under shear, rather than acting as rigid chains.

Table 4. Best fitting parameters to the viscosity curves corresponding to Eq. (2) in the case of a 2.8 vol %, S7 composite ferrofluid.

H_0 (kA/m)	c (Pa·s^2)	n	η_∞ (Pa·s)
27	1676	0.74	12.8
67	4328	0.79	13
134	6678	0.79	12.5
201	8559	0.8	12.4
267	9823	0.81	12.2
401	11245	0.79	12.4

Since magnetostatic and hydrodynamic forces are considered as the dominant factors governing magnetorheological behavior, an initial attempt to obtain a master flow curve was made using $\dot{\gamma}/H^2$ scaling. However, as shown in Fig.8, this simple scaling approach did not yield satisfactory fitting results, primarily because it fails to account for the magnetic properties of the two phases present in the ferrofluid.

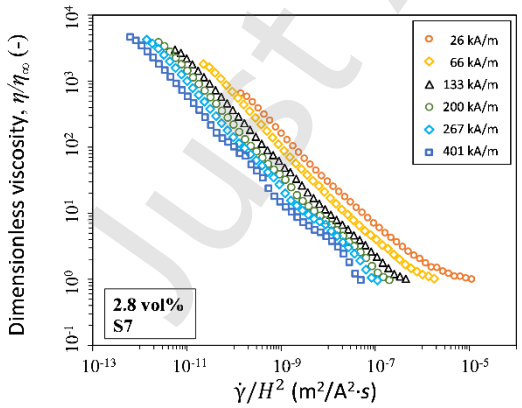

Fig.8 Dimensionless viscosity curves (η/η_∞) as a function of $\dot{\gamma}/H^2$, derived from the data presented in Fig.7.

The formation of field-induced structures in ferrofluids originates from the magnetic permeability contrast between the dispersed and continuous phases in the composite system. This contrast is commonly characterized by the contrast factor (also referred to as the coupling parameter) β, defined as: $\beta = (\mu_{pr} - \mu_{cr})/(\mu_{pr} + 2\mu_{cr})$, where μ_{pr} and μ_{cr} represent the relative magnetic permeabilities of the dispersed and continuous phases, respectively. In the present study, hydrophilic fumed silica is introduced into a water-based ferrofluid. As the silica

Just Accepted

does not physically integrate with the magnetic nanoparticles nor form a percolated network (i.e., no gelation occurs), it remains in a dispersed state. Therefore, the hydrophilic silica can be considered the dispersed phase, while the ferrofluid acts as the continuous phase. Since silica is a nonmagnetic material, its relative permeability μ_{pr} is approximately equal to 1. Substituting into the expression for β yields: $\beta = (1 - \mu_{cr})/(1 + 2\mu_{cr})$.

Under an applied magnetic field, the value of β reflects the strength of interparticle magnetic interactions. A lower β—typically associated with ferrofluids of low permeability or under weak magnetic fields—indicates weaker interactions among magnetic particles. In such cases, the formation of chain-like structures spanning the fluid layer can only occur under small gap conditions, enabling noticeable magnetorheological enhancement. Conversely, when the gap is large, these structures may not fully bridge the shear region, resulting in limited macroscopic rheological response[66]. In practical systems, β usually ranges between –0.5 (in low-field conditions) and 0 (in strong fields). Notably, achieving a low β value is challenging and often requires extremely narrow geometric gaps to facilitate the formation of field-induced structures across the entire gap.

To further quantify the coupling between the magnetic field and shear flow, a dimensionless parameter known as the Mason number (Mn), which incorporates β, is defined as follows:

$$\mathrm{Mn} = \frac{8\eta_c\dot{\gamma}}{\mu_0\mu_{cr}\beta^2H^2} \tag{3}$$

Where η_c is continuous phase (ferrofluid) viscosity, $\dot{\gamma}$ is the shear rate, μ_0 is the permeability of vacuum, and H is the magnetic field strength. The Mason number (Mn) which is a dimensionless shear rate that can be defined as the ratio of (Stokesian) hydrodynamic forces to (dipolar) magnetostatic forces, and it is a key parameter for understanding the structural evolution and flow behavior of magnetorheological systems. As shown in Fig.9, a master curve was obtained by rescaling the shear viscosity data of the composite ferrofluid containing 2.8 vol% S7 silica (from Fig.7) under various magnetic field strengths using the Mason number (Mn). Here, η/η_∞ represents the dimensionless viscosity as a function of Mn. According to the previous analysis by Marshall et al.[67], for a given volume fraction, the dimensionless viscosity can be expressed as a function of the Mason number:

$$\frac{\eta}{\eta_\infty} = 1 + \mathrm{Mn}^*(\phi) \cdot \mathrm{Mn}^{\Delta}, \tag{4}$$

Here, η_∞ represents the field-independent high-shear viscosity, and $\mathrm{Mn}^*(\phi)$ is the critical Mason number, which characterizes the transition from magnetization to hydrodynamic control of system structure. It is defined as: $\mathrm{Mn}^*(\phi) = C\phi\eta_c/\eta_\infty$, where C is a structural factor that reflects the strength of interparticle interactions within the system. $\mathrm{Mn}^*(\phi)$ contains the volume fraction dependence of magnetorheology fluids under flow and corresponds to the intersection of the linear fall of the log (η/η_∞) versus log Mn with the horizontal line representing the high-shear viscosity plateau.

As shown in Fig.9, a good data collapse is achieved over approximately seven orders of magnitude of the Mason number. The black solid line in the figure represents the theoretical values obtained from Eq. (4), indicating that the Mason number effectively captures the combined influence of shear rate and magnetic field strength on the system in this study. This further suggests that, in such composite ferrofluid, thermodynamic and colloidal forces can be considered negligible.

Just Accepted

To more comprehensively assess the validity of the experimental results, Fig.9 also includes a comparison with two representative theoretical models. The red dashed line corresponds to the ideal chain-structure model proposed in Ref.[64], which assumes rigid fracture of chain-like aggregates under shear, yielding a power-law relationship of $\eta \propto \mathrm{Mn}^{-1}$. In this model, the exponent is defined as $\Delta = -1$, indicating a high sensitivity of the structure to shear. In contrast, the viscosity decline in the present study is more gradual, suggesting that the field-induced structures possess flexibility and undergo progressive deformation and breakdown rather than abrupt rupture during shear.

The blue dash-dotted line in Fig.9 represents the theoretical values proposed from Ref.[35] , which is also based on Eq. (4). In that study, micron-sized hydrophobic silica was added to an oil-based ferrofluid, while the present work employs nanoscale hydrophilic silica in a water-based system. The two systems exhibit similar power-law exponents ($\Delta = -0.76$ and $\Delta = -0.75$), indicating comparable structural breakdown mechanisms. However, their critical Mason numbers differ significantly: Mn* = 0.141 in Ref.[35], compared to Mn* = 3.96 in this study, This indicates that structure formed in the present system are more compact and stable, and require stronger shear or magnetic field input for their formation.

As Mn further increases, hydrodynamic forces begin to dominate over magnetostatic interactions, and the dimensionless viscosity levels off. Eventually, the field-induced structures are destroyed under shear flow. The Mason number corresponding to the breakage of the last doublet under shear is given by[68]

$$\mathrm{Mn}_b = \frac{1.581\sqrt{f_{\parallel} f_{\Gamma}}}{\sqrt{2.038 + \frac{0.8 f_{\perp}}{f_{\Gamma}}}} \tag{5}$$

Under the dipole approximation, all f functions in Eq. (17) can be approximated as unity 1 and the $\mathrm{Mn}_b \approx 0.94$. As shown in Fig.9, this value qualitatively coincides with the onset of the high-shear plateau region.

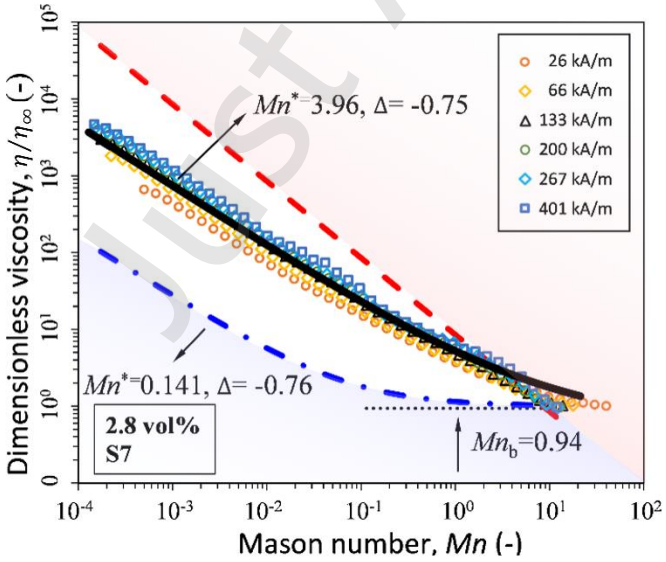

Fig.9 Dimensionless viscosity curves (η/η_∞) from Fig.7 as a function of Mason number (Mn). Lines represent theoretical models: black solid line, the best fit based on Eq. (4) to with $\mathrm{Mn}^* = 3.96$ and exponent $\Delta = -0.75$; dash line, $\eta_F \propto Mn^{-1}$ from Ref.[64] ; dash-dotted line, Eq. (4) with $\mathrm{Mn}^* = 0.141$ and exponent $\Delta = -0.76$ from Ref.[35]; and black dotted line, Eq. (5).

Just Accepted

Fig.10 presents the dimensionless viscosity curves (η/η_∞) as a function of the Mason number (Mn) for composite ferrofluid containing different volume fractions of S7 fumed silica (Φ=1.1 vol%, 1.7 vol%, and 2.8 vol%). All samples exhibit shear-thinning trend, and the critical Mason number Mn* increases with increasing silica concentration. This indicates that the higher the concentration of fumed silica, the greater the shear-resistant stability of the system, possibly due to spatial confinement effect of the nonmagnetic silica, which limits the mobility of magnetic particles within the chains and thereby stabilizes the field-induced structure.

Meanwhile, the absolute value of the power-law exponent Δ also increases with silica content (from –0.58 to –0.75), indicating a stronger shear-thinning response and a trend toward the behavior predicted by the ideal chain model (Δ = –1). This behavior may be attributed to the decreased structural flexibility of magnetic chains at higher silica concentrations, where nonmagnetic particles reduce the ability of the structure to reconstruct under shear. As a result, the structures are more prone to shear-induced disintegration, leading to a sharper viscosity decline.

In summary, increasing the concentration of fumed silica enhances the stability of magnetic chain structures, as evidenced by a higher critical Mason number (Mn*), but once the critical threshold is exceeded, they are more susceptible to breakdown (as reflected by the larger absolute value of Δ), resulting in a more pronounced shear-thinning behavior. This suggests that while hydrophilic fumed silica particles enhance the structural stability, they also weaken the system's cooperative resistance to shear.

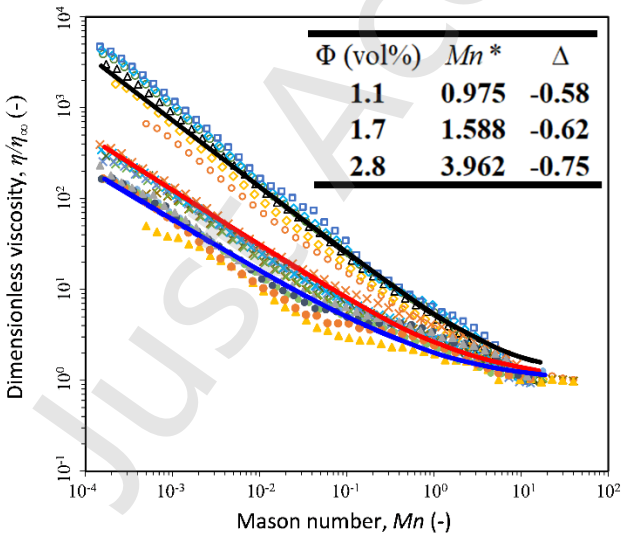

Fig.10 Master curves of dimensionless viscosity (η/η_∞) as a function of Mason number (Mn) for composite ferrofluids containing S7 hydrophilic fumed silica at different volume fractions: closed symbols, 1.1 vol%; crossed symbols, 1.7 vol%; open symbols, 2.8 vol%. All measurements were conducted under varying magnetic field strengths (same as in Fig.9). Solid lines represent theoretical values from Eq. (4) for each concentration. Fitting parameters are listed in the inset table.

Fig.11 shows the effect of hydrophilic fumed silica particle size on the rheological behavior of composite ferrofluids at a fixed volume fraction of 2.8 vol%. Two types of silica were investigated: S7 (≈7 nm) and S14 (≈14 nm). Experimental data were scaled by Mn to generate

Just Accepted

master curves of dimensionless viscosity (η/η_∞). Both samples exhibit good collapse and shear-thinning behavior.

As the silica particle size increases, the critical Mason number Mn* increases with particle size, from 2.594 for S7 to 3.962 for S14. This indicates that systems containing larger particles require higher Mason numbers (i.e., stronger hydrodynamic forces relative to magnetic force) to initiate structural breakdown. This phenomenon may be attributed to the larger silica particles occupying more space in the suspension and locally supporting the magnetic chain structures, thereby improving their resistance to shear.

In contrast, the silica particle size has little effect on the power-law exponent Δ. with both systems yielding Δ = –0.62, indicating a similar degree of shear thinning and a consistent structural breakdown mechanism. This finding is in agreement with storage modulus investigations by Ref[34] , further supporting the reliability of the observed phenomenon.

In summary, larger silica particle size enhances the stability of magnetic chain structures, as reflected by the higher Mn*. This is likely due to improved local support for the chain-like structure from the larger particles. However, the shear-thinning behavior remains unchanged (Δ = –0.62), indicating that particle size has little effect on the structural breakdown mechanism.

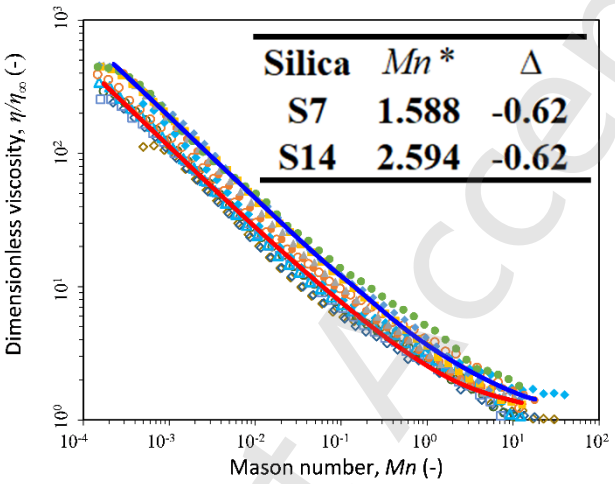

Fig.11 Master curves of dimensionless viscosity (η/η_∞) as a function of Mason number (Mn) for composite ferrofluids containing hydrophilic fumed silica of different particle sizes: closed symbols, S14; open symbols, S7. Measurements were conducted under varying magnetic field strengths (same as in Fig.9). Solid lines represent fits to Eq. (4), and the corresponding fitting parameters are listed in the inset table.

3.3 Yield behavior

Apart from flow behavior, yield stress is another critical rheological property of ferrofluids. It refers to the minimum stress required to initiate substantial deformation or flow. As it is generally proportional to the force needed to disrupt field-induced structures, yield stress is especially important in applications involving torque transmission.

Currently, the most widely used method for determining yield stress is an indirect approach, in which the post-yield region of the flow curve is fitted using classical viscoplastic fluid models such as the Bingham, Herschel–Bulkley, or Casson equations. In this study, the Bingham model was selected due to its suitability for capturing the flow behavior of ferrofluids undergoing continuous disruption. Furthermore, the linear post-yield assumption of the Bingham model shows good agreement with the experimental flow behavior throughout the yielded region[69], as demonstrated

Just Accepted

in Fig.7. The Bingham model is defined as:

$$\begin{aligned} \tau(\dot{\gamma}, H) &= \tau_{y,B}(H) + \eta_p \dot{\gamma} \quad \text{for } \tau > \tau_0, \\ \dot{\gamma} &= 0 \qquad\qquad\quad \text{for } \tau < \tau_0. \end{aligned} \tag{6}$$

where $\tau_{y,B}(H)$ is the Bingham yield stress, which is often referred to as the "dynamic yield stress" in magnetorheological literature. It denotes the minimum stress needed to continuously break the aggregates which reform in the presence of the magnetostatic forces[62]. Yield stress depends on the interparticle interaction potential, which is primarily governed by dipole–dipole magnetic interactions and is proportional to the square of the applied magnetic field strength. To enable comparison under different magnetic field conditions, the yield stress is normalized in this study as: $\tau_{y,n} = \tau_y/(\mu_0 \mu_{cr} H_0^2)$.

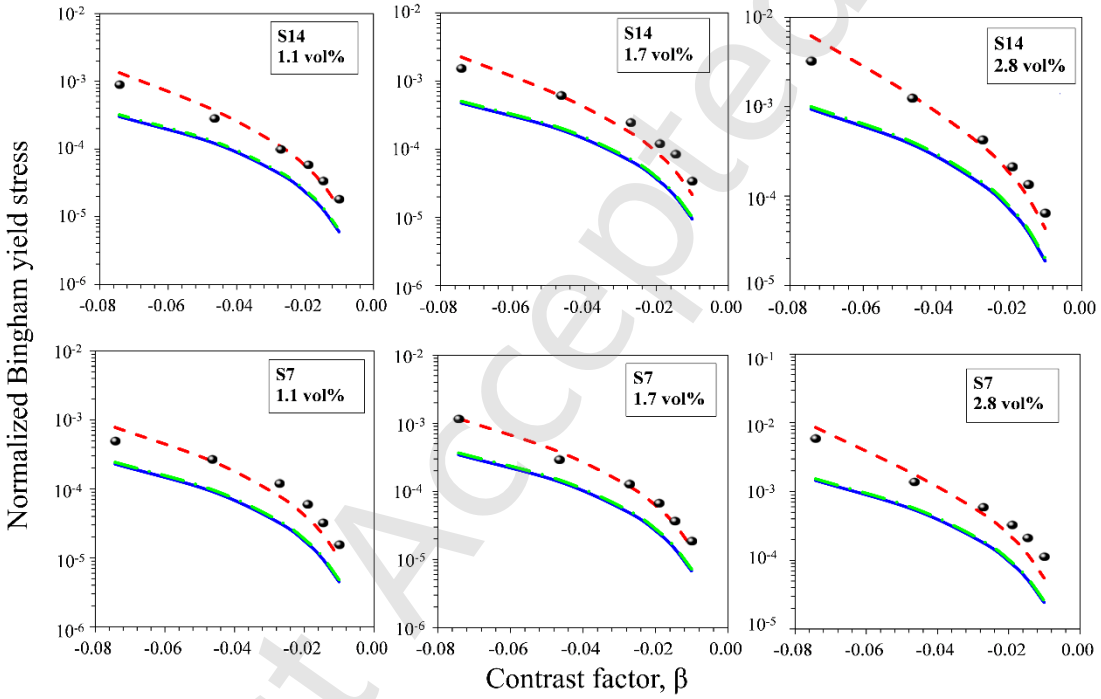

Fig.12 Comparison between experiments and macroscopic theoretical models for composite ferrofluids with different silica particle size (S7 and S14) at three different particle volume fractions (1.1, 1.7, 2.8 vol%). Black solid circle, normalized Bingham yield stress; blue solid line, spheroidal model (Eq.8); red dashed line, layered aggregates model (Eq.9, with C=1); green dash-dotted line, cylindrical model (Eq. 9 with C=2).

As shown in Fig.12, the normalized Bingham yield stress was obtained experimentally for composite ferrofluids with different particle sizes of hydrophilic fumed silica (S7 and S14) and volume fractions (1.1, 1.7, and 2.8 vol%). To better understand the structural mechanisms behind the observed yield behavior, several macroscopic yield stress models based on magnetic energy minimization were employed for comparison and interpretation. These models have been demonstrated to effectively predict the Bingham yield behavior of composite ferrofluids[70]. In these models, the ferrofluid is treated as a continuous medium, with shear stress arising mainly from magnetostatic interactions between nonmagnetic particles, and the system is assumed to deform affinely under shear. In addition, to simplify the modeling, the interactions between different field-induced aggregates are neglected, making the models most applicable to low particle concentrations.

Just Accepted

Basically, these models are based on a mesoscopic description of the structure only taking into account the shape anisotropy of the strained aggregates under small deformation. Internal structure within the aggregates is ignored and only the particle volume fraction inside is required as input in the models. For the purposes of this study, ϕ_a is assumed to be approximately 4, corresponding to a random close packing structure. Only minor variations in the results are observed when different values of ϕ_a are used. When subjected to shear, the aggregates deviate from alignment with the applied magnetic field direction, leading to a decrease in magnetic energy and generating a restoring stress τ, which can be estimated as follows:

$$\tau = -\frac{\partial W}{\partial \gamma}, \tag{7}$$

here, W denotes the magnetostatic energy density, and γ is the shear strain. The yield stress can be obtained by taking the maximum value of the resulting stress expression.

To account for different aggregate morphologies, this study analyzes yield stress models corresponding to various structural forms, including spheroidal, cylindrical, and layered aggregates. For the spheroidal aggregate model, the aspect ratio is set to 10, and the demagnetization factors along the directions parallel and perpendicular to the magnetic field are denoted as n_1 and n_2, respectively. The expression for the normalized yield stress is given by:

$$\tau_{y,n,S} = -0.325\phi_s \frac{1+2\phi\beta}{1-\phi\beta}\tilde{\mu}_a\left(\frac{1}{1+\tilde{\mu}_a n_2} - \frac{1}{1+\tilde{\mu}_a n_1}\right), \tag{8}$$

here, $\phi_s = \phi/\phi_a$ represents the ratio between the non-magnetic particle volume fraction (e.g., added hydrophilic fumed silica) fraction and the internal volume fraction within field-induced aggregates. The relative permeability contrast between the aggregate (μ_a) and the composite ferrofluid (μ) is quantified by $\tilde{\mu}_a = \mu_a/\mu - 1$, To estimate magnetic permeability, the Maxwell Garnett mean field theory[71] is adopted. Under this approximation, the effective permeability of the aggregates is given by: $\mu_a = \mu_c(1+2\beta\phi_a)/(1-\beta\phi_a)$ and the composite ferrofluid $\mu = \mu_c(1+2\beta\phi)/(1-\beta\phi)$, where ϕ is the non-magnetic particle volume fraction. The applicability of Maxwell Garnett's theory to composite ferrofluids was confirmed by Volkova et al.[62]. Furthermore, Bossis et al.[70] extended the shear stress model originally proposed by Rosensweig[72] to describe ordered magnetic structures in the form of cylindrical and layered aggregates. The corresponding normalized yield stress can be expressed as:

$$\tau_{y,n,\frac{C}{L}} = 0.325\phi_s\left(\frac{\mu_a}{\mu_c}-1\right)^2 \frac{1-\phi_s}{C+\left(\frac{\mu_a}{\mu_c}-1\right)(1-\phi_s)}, \tag{9}$$

where $C = 2$ for the case of cylinder-like aggregates and $C = 1$ for the case of layered aggregates. Fig.12 compares the normalized experimental yield stress with predictions from three macroscopic models under varying silica particle sizes (S7 and S14) and volume fractions (1.1, 1.7, and 2.8 vol%). Among the models, the layered aggregates model consistently shows the best agreement with the experimental data, indicating that the field-induced structures in the composite ferrofluids are more likely to adopt a layered morphology. This structural arrangement leads to yield behavior that is well described by magnetic energy variations within such layered configurations.

Just Accepted

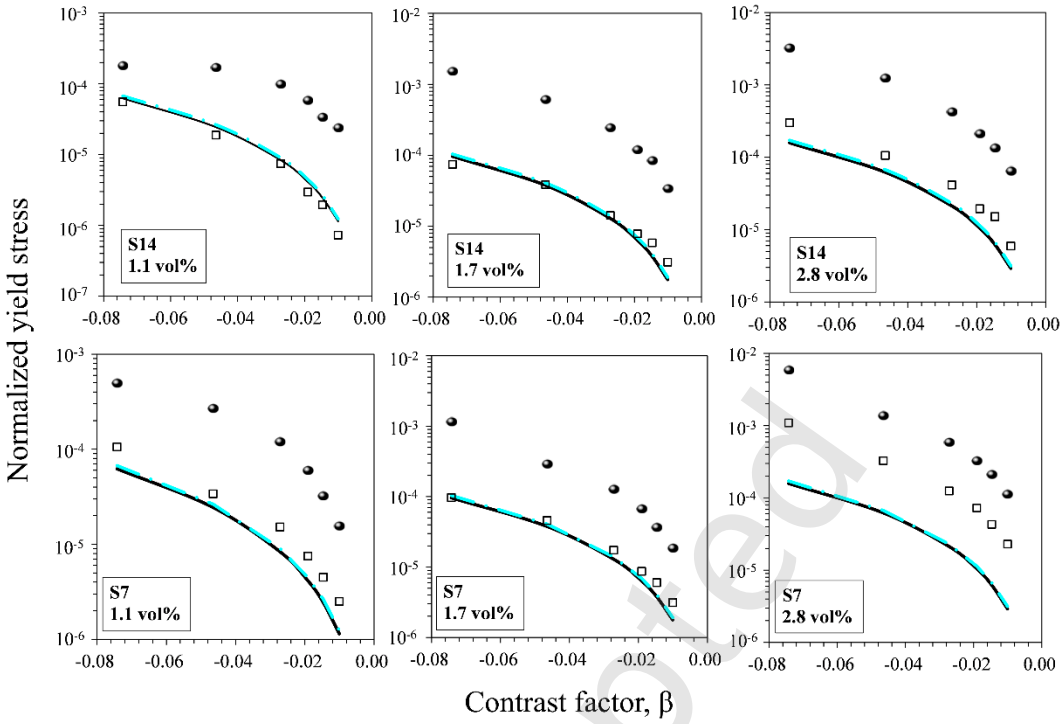

Fig.13 Comparison between experiments and microscopic theoretical models for composite ferrofluids with different silica particle sizes (S7 and S14) at three different particle volume fractions (1.1, 1.7, 2.8 vol%). Black solid circle, normalized Bingham yield stress; open squares, normalized static yield stress; black solid line, particle-pair model, Eq. 13; cyan dash-dotted line, chain model, Eq.15.

To better understand the yielding behavior, this study also examined the static yield stress (or frictional yield stress), which is associated with the initial slip of particle aggregates along the shear plate and marks the onset of structural motion. This value is typically lower than the dynamic yield stress defined by the Bingham model. It was determined by fitting the low shear-rate region of the flow curve and extrapolating the stress to zero shear rate. Figure 13 presents the measured static and dynamic yield stresses, both expressed as normalized yield stress for consistent comparison.

Unlike the macroscopic models in Fig.12, which are based on aggregate-level morphology and magnetic energy minimization, the two models in Fig.13 are derived from magnetostatic interactions between individual particles using microscopic mechanical principles.

The first model, proposed in Ref.[73], is based on a multipole expansion of the interaction force between two isolated magnetizable spheres and yields the following expression:

$$F_m = -12\pi\mu_0\mu_{cr}\beta^2 a^2 H^2 \left(\frac{a}{r}\right)^4 \left[\left(2f_{\parallel}\cos^2\theta - f_{\perp}\sin^2\theta\right)\hat{r} + \left(f_{\Gamma}\sin 2\theta\right)\hat{\theta}\right], \qquad (10)$$

where a is the particle radius; r is the center-to-center distance; $f_{\parallel}$, $f_{\perp}$, and f_{Γ} are the parallel, perpendicular, and gamma coefficients, respectively; $\hat{r}$ and $\hat{\theta}$ represent the radial and tangential unit vectors, respectively. The horizontal component of the force required to separate two particles under affine deformation and dipolar approximation (i.e., $f_{\parallel} = f_{\perp} = f_{\Gamma} = 1$) is given by

$$F_H = 12\pi\mu_0\mu_{cr}\beta^2 a^2 H^2 f_m, \qquad (11)$$

where $f_m = 0.057$ corresponds to a yield strain of $\gamma_{y,KZ} = \tan(\theta_{max}) = \tan(0.371) = 0.389$, and hence, a first approximation to the yield stress is

Just Accepted

$$\tau_y = \frac{N_C F_H}{S}, \tag{12}$$

where $N_C/S = 3\phi/2\pi a^2$ is the number of chains per unit surface of the plate. As a consequence, substituting Eq. (11) to Eq. (12), a simple equation for the normalized yield stress results that predicts a quadratic dependence:

$$\tau_{y,n,\frac{C}{L}} = 1.026\phi\beta^2. \tag{13}$$

The second model[61] assumes non-interacting particle chains that undergo affine deformation and are rigidly fixed to the shearing surfaces. With each particle in static equilibrium, the shear stress is calculated based on the force acting on a single particle. The resulting expression is:

$$\tau = \frac{9}{8}\zeta(4)\phi\mu_0\mu_{cr}\beta^2 H^2[\sin\theta\cos^4\theta(5\cos^2\theta - 1)], \tag{14}$$

where $\zeta(4) = \Sigma_{n=1}^{\infty} n^{-4} = \pi^4/90$ denotes Riemann's zeta function. This equation reaches its maximum at a yield strain of $\gamma_{y,dG1} = 0.389$ consistent with the previous model. The corresponding normalized yield stress is given by:

$$\tau_{y,n,dG1} = 1.11\phi\beta^2. \tag{15}$$

Both microscopic mechanical models predict that the yield stress increases linearly with the particle volume fraction ϕ of fumed silica and quadratically with the magnetic contrast factor β.

As shown in Fig.13, both normalized Bingham (solid circles) and static yield stresses (open squares) increase with increasing silica concentration for both S7 and S14 systems. The microscopic model predictions agree well with the normalized static yield stress at 1.1 and 1.7 vol%, whereas at 2.8 vol% the experimental values are higher than the theoretical ones. This deviation can be attributed to enhanced particle–particle friction, multiparticle geometric constraints, and non-affine rearrangements, none of which are accounted for in the microscopic models.

Moreover, all normalized Bingham yield stresses (normalized dynamic yield stresses) in Fig. 13 significantly exceed the normalized static yield stresses, this difference between dynamic and static yielding has also been widely reported in MR/ER systems[61][70]. The static yield stress corresponds to the onset of slip, where only the initial dipolar binding forces must be overcome, in contrast, the dynamic (Bingham) yield stress reflects the average stress required to maintain continuous flow under steady shear, which involves the repeated breakage and reformation of field-induced aggregates. The additional stress associated with this restructuring explains why dynamic yield stresses consistently exceed static ones.

This distinction also explains why macroscopic and microscopic yield-stress models differ in their applicability. The macroscopic (energy-based) models approximate field-induced aggregates as a continuum and calculate shear stress from magnetic energy variations. They are better suited to describe the dynamic (Bingham) yield stress during continuous flow, where aggregates are repeatedly broken and reformed. The normalized form ($\tau_{y,n} = \tau_y/(\mu_0\mu_{cr}H_0^2)$) directly captures the field-dependent energy scale of this process, which explains its consistency with both classical ER/MR results[70] and silica-modified MR suspensions, where silica increases the mean resistance but the post-yield slope remains governed by magnetic energy scaling[74]. In contrast, the microscopic (pair/chain) model is better able to capture the static yield stress that arises from actual particle–particle contact rupture, they are therefore more closely linked to the structural stability at the yield threshold and show better agreement with the static yield stress. At higher silica concentrations, however, multiparticle constraints, frictional contacts, and non-affine

Just Accepted

rearrangements—effects not included in the classical microscopic frameworks—lead to an underestimation of the measured static yield stress. When the silica concentration exceeds ~3.8 vol% (Fig. 6b), the formation of a three-dimensional particle network introduces additional stresses, and both Mason-number scaling and microscopic models require modification. Future work could extend the present analysis to gelled ferrofluids, where network-induced stresses are explicitly considered.

4. Conclusion

This study systematically studied the influence of hydrophilic fumed silica on the steady shear rheological behavior of water-based ferrofluids under different magnetic field strengths, with particular attention to avoiding gelation that reduces fluidity. The result shows that Mason number scaling successfully unified the rheological responses under different magnetic fields, indicating that magnetic and hydrodynamic interactions dominate over thermodynamic and colloidal forces. Furthermore, Higher silica concentration or particle size increases the critical Mason number, reflecting more stable field-induced structures. although high concentrations also promote stronger shear-thinning, while particle size has little effect on flow index (|Δ|). Yield stress analysis further revealed that macroscopic models well describe normalized Bingham yield stress, while microscopic models better capture normalized static yield stress, highlighting distinct yielding mechanisms. Overall, by revealing water–silica interactions, linking rheological data with macroscopic and microscopic yield-stress models, and proposing a simple experimental route for rheology control without gelation, this work highlights a practical strategy for designing stable and tunable magnetically responsive fluids.

5. References

[1] Odenbach S. Colloidal Magnetic Fluids[M]. Springer Berlin Heidelberg, 2009.

[2] Rosensweig. Ferrohydrodynamics[M]. Cambridge University Press, 1985.

[3] Pu S, Chen X, Chen L, et al. Tunable magnetic fluid grating by applying a magnetic field[J]. Applied Physics Letters, 2005, 87(2): 10-13.

[4] Philip J, Jaykumar T, Kalyanasundaram P, et al. A tunable optical filter[J]. Measurement Science and Technology, 2003, 14(8): 1289-1294.

[5] Mahendran V, Philip J. Nanofluid based optical sensor for rapid visual inspection of defects in ferromagnetic materials[J]. Applied Physics Letters, 2012, 100(7): 51-54.

[6] Odenbach S. Recent progress in magnetic fluid research[J]. Journal of physics: condensed matter, 2004, 16(32): R1135.

[7] Mitamura Y, Arioka S, Sakota D, et al. Application of a magnetic fluid seal to rotary blood pumps[J]. Journal of Physics Condensed Matter, 2008, 20(20).

[8] Shima P D, Philip J. Tuning of thermal conductivity and rheology of nanofluids using an external stimulus[J]. The Journal of Physical Chemistry C, 2011, 115(41): 20097-20104.

[9] Philip J, Shima P D, Raj B. Enhancement of thermal conductivity in magnetite based nanofluid due to chainlike structures[J]. Applied physics letters, 2007, 91(20).

[10] Jain T K, Richey J, Strand M, et al. Magnetic nanoparticles with dual functional properties: drug delivery and magnetic resonance imaging[J]. Biomaterials, 2008, 29(29): 4012-4021.

[11] Shokrollahi H. Structure, synthetic methods, magnetic properties and biomedical

Just Accepted

applications of ferrofluids[J]. Materials Science and Engineering: C, 2013, 33(5): 2476-2487.

[12] Pablico-Lansigan M H, Situ S F, Samia A C S. Magnetic particle imaging: advancements and perspectives for real-time in vivo monitoring and image-guided therapy[J]. Nanoscale, 2013, 5(10): 4040-4055.

[13] Khan H A. The Study of Magnetic Field Effect on Two-Phase Liquid-Gas Ferrofluid Flow inside the Microchannel for Spacecraft Applications[M]. Khalifa University of Science, 2022.

[14] Moskowitz R. Technology ferrofluids: Liquid magnetics: A space-age research spin-off finds its way out of the laboratory and into a host of lubricating and damping applications[J]. IEEE spectrum, 1975, 12(3): 53-57.

[15] Yang W, Zhang Y, Yang X, et al. Systematic analysis of ferrofluid: a visualization review, advances engineering applications, and challenges[J]. Journal of Nanoparticle Research, 2022, 24(6): 102.

[16] Raj K, Moskowitz R. A review of damping applications of ferrofluids[J]. IEEE Transactions on Magnetics, 1980, 16(2): 358-363.

[17] Sohail A, Fatima M, Ellahi R, et al. A videographic assessment of ferrofluid during magnetic drug targeting: an application of artificial intelligence in nanomedicine[J]. Journal of Molecular Liquids, 2019, 285: 47-57.

[18] Amiri H, Bustamante R, Millán A, et al. Magnetic and relaxation properties of multifunctional polymer-based nanostructured bioferrofluids as MRI contrast agents[J]. Magnetic Resonance in Medicine, 2011, 66(6): 1715-1721.

[19] Eberle A P R, Wagner N J, Castaneda-Priego R. Dynamical arrest transition in nanoparticle dispersions with short-range interactions[J]. Physical review letters, 2011, 106(10): 105704.

[20] Stefan Odenbach. Magnetoviscous Effects in Ferrofluids[M]//Springer Berlin Heidelberg. Bremen.

[21] Felicia L J, Vinod S, Philip J. Recent Advances in Magnetorheology of Ferrofluids (Magnetic Nanofluids)—A Critical Review[J]. Journal of Nanofluids, 2015, 5(1): 1-22.

[22] Li Q, Li D, Zhang S, et al. Synthesis and rheological properties of water-based Fe3O4 magnetic fluid[J]. Physics of Fluids, 2024, 36(3).

[23] López-López M T, Gómez-Ramírez A, Rodríguez-Arco L, et al. Colloids on the frontier of ferrofluids. Rheological properties[J]. Langmuir, 2012, 28(15): 6232-6245.

[24] Kim Y J, Liu Y D, Seo Y, et al. Pickering-emulsion-polymerized polystyrene/Fe2O3 composite particles and their magnetoresponsive characteristics[J]. Langmuir, 2013, 29(16): 4959-4965.

[25] Sun L, Zhang Y, Cui X, et al. Magnetic lubricants: preparation, physical mechanism, and application[J]. Friction, 2025, 13(7): 9441010.

[26] Zhu X, Jing X, Cheng L. Magnetorheological fluid dampers: A review on structure design and analysis[J]. Journal of intelligent material systems and structures, 2012, 23(8): 839-873.

[27] Goldowsky M. New methods for sealing, filtering and lubricating with magnetic fluids[J]. IEEE Transactions on magnetics, 2003, 16(2): 382-386.

[28] Wang X, Zhao Y, Liu H, et al. Influence of external magnetic field on the tribological performance of magnetic fluids in different lubrication regimes[J]. Friction, 2025,

Just Accepted

13(7): 9440979.

[29] Kang K, Lee L J, Koelling K W. High shear microfluidics and its application in rheological measurement[J]. Experiments in fluids, 2005, 38: 222-232.

[30] Du C, Li M, Cao M, et al. Enhanced thermal and mechanical properties of polyvinlydene fluoride composites with magnetic oriented carbon nanotube[J]. Carbon, 2018, 126: 197-207.

[31] Paul P S, Iasanth J A, Vasanth X A, et al. Effect of nanoparticles on the performance of magnetorheological fluid damper during hard turning process[J]. Friction, 2015, 3(4): 333-343.

[32] Wu Z, Mueller A, Degenhard S, et al. Enhancing the magnetoviscosity of ferrofluids by the addition of biological nanotubes[J]. ACS nano, 2010, 4(8): 4531-4538.

[33] Skjeltorp A T. One-and two-dimensional crystallization of magnetic holes[J]. Physical Review Letters, 1983, 51(25): 2306.

[34] De Gans B J, Duin N J, Van Den Ende D, et al. The influence of particle size on the magnetorheological properties of an inverse ferrofluid[J]. Journal of Chemical Physics, 2000, 113(5): 2032-2042.

[35] Ramos J, Klingenberg D J, Hidalgo-Alvarez R, et al. Steady shear magnetorheology of inverse ferrofluids[J]. Journal of Rheology, 2011, 55(1): 127-152.

[36] Ramos J, De Vicente J, Hidalgo-Alvarez R. Small-amplitude oscillatory shear magnetorheology of inverse ferrofluids[J]. Langmuir, 2010, 26(12): 9334-9341.

[37] Raghavan S R, Walls H J, Khan S A. Rheology of silica dispersions in organic liquids: New evidence for solvation forces dictated by hydrogen bonding[J]. Langmuir, 2000, 16(21): 7920-7930.

[38] Khan S A, Zoeller N J. Dynamic rheological behavior of flocculated fumed silica suspensions[J]. Journal of Rheology, 1993, 37(6): 1225-1235.

[39] Chen B, Yang M, Fan C, et al. Effect of silica morphology on rheological properties and stability of magnetorheological fluid[J]. Functional Materials Letters, 2023, 16(07): 2340030.

[40] Zhang Y, Jiang J, Ouyang C, et al. Effect of nano-silica-particle additive on magneto-rheological behavior[J]. Rheologica Acta, 2022, 61(11): 785-798.

[41] De Vicente J, López-López M T, González-Caballero F, et al. Rheological study of the stabilization of magnetizable colloidal suspensions by addition of silica nanoparticles[J]. Journal of Rheology, 2003, 47(5): 1093-1109.

[42] Alves S, Alcantara M R, Figueiredo Neto A M. The effect of hydrophobic and hydrophilic fumed silica on the rheology of magnetorheological suspensions[J]. Journal of Rheology, 2009, 53(3): 651-662.

[43] Felicia L J, Philip J. Effect of hydrophilic silica nanoparticles on the magnetorheological properties of ferrofluids: A study using opto-magnetorheometer[J]. Langmuir, 2015, 31(11): 3343-3353.

[44] Imran M, Affandi A M, Alam M M, et al. Advanced biomedical applications of iron oxide nanostructures based ferrofluids[J]. Nanotechnology, 2021, 32(42): 422001.

[45] Martins P M, Lima A C, Ribeiro S, et al. Magnetic nanoparticles for biomedical applications: from the soul of the earth to the deep history of ourselves[J]. ACS Applied Bio Materials, 2021, 4(8): 5839-5870.

[46] Kole M, Khandekar S. Engineering applications of ferrofluids: A review[J]. Journal

Just Accepted

of Magnetism and Magnetic Materials, 2021, 537: 168222.

[47] Yoshimura A, Prud'homme R K. Wall Slip Corrections for Couette and Parallel Disk Viscometers[J]. Journal of Rheology, 1988, 32(1): 53-67.

[48] Bossis G, Volkova O, Lacis S, et al. Magnetorheology: Fluids, Structures and Rheology[J]. 2002: 202-230.

[49] Maurya C S, Sarkar C. Magnetorheological fluids: a comprehensive review of operational modes and performance under varied circumstances[J]. Rheologica Acta, 2024, 63(11-12): 765-785.

[50] Rodrigues R, Galindo-Rosales F J, Campo-Deaño L. Effects of non-parallelism on standard and magnetorheological measurements[J]. arXiv preprint arXiv:2502.20967, 2025.

[51] Zhu Y, McNeary M, Breslin N, et al. Effect of structures on rheology in a model magnetorheological fluid[J]. International Journal of Modern Physics B, 1999, 13(14n16): 2044-2051.

[52] Brunn P O, Asoud H. Analysis of shear rheometry of yield stress materials and apparent yield stress materials[J]. Rheologica acta, 2002, 41(6): 524-531.

[53] Ferrari E F, Da Silva F C S, Knobel M. Influence of the distribution of magnetic moments on the magnetization and magnetoresistance in granular alloys[J]. Physical Review B, 1997, 56(10): 6086.

[54] Li J, Dai D, Liu X, et al. Preparation and characterization of self-formed CoFe2O4 ferrofluid[J]. Journal of materials research, 2007, 22(4): 886-892.

[55] Bailey J R, McGuire M M. ATR-FTIR observations of water structure in colloidal silica: Implications for the hydration force mechanism[J]. Langmuir, 2007, 23(22): 10995-10999.

[56] Mewis J, Wagner N J. Colloidal suspension rheology[M]. Cambridge university press, 2012.

[57] Winter H H, Chambon F. Analysis of linear viscoelasticity of a crosslinking polymer at the gel point[J]. Journal of rheology, 1986, 30(2): 367-382.

[58] Macosko C W. Rheology principles[J]. Measurements and Applications, 1994.

[59] Rueb C J, Zukoski C F. Rheology of suspensions of weakly attractive particles: Approach to gelation[J]. Journal of Rheology, 1998, 42(6): 1451-1476.

[60] Shih W H, Shih W Y, Kim S I, et al. Scaling behavior of the elastic properties of colloidal gels[J]. Physical review A, 1990, 42(8): 4772.

[61] De Gans B J, Hoekstra H, Mellema J. Non-linear magnetorheological behaviour of an inverse ferrofluid[M]//Faraday Discussions. 1999: 209-224. https://doi.org/10.1039/a809229j.

[62] Volkova O, Bossis G, Guyot M, et al. Magnetorheology of magnetic holes compared to magnetic particles[J]. Journal of Rheology, 2000, 44(1): 91-104.

[63] Felt D W, Hagenbuchle M, Liu J, et al. Rheology of a magnetorheological fluid[J]. Journal of Intelligent Material Systems and Structures, 1996, 7(5): 589-593.

[64] Vicente J De, Lo M T, Dura J D G, et al. Shear flow behavior of confined magnetorheological fluids at low magnetic field strengths[J]. 2004: 94-103.

[65] Halsey T C, Martin J E, Adolf D. Rheology of Electrorheological Fluids[J]. 1992.

[66] Andablo-Reyes E, Hidalgo-Álvarez R, De Vicente J. Controlling friction using magnetic nanofluids[J]. Soft Matter, 2011, 7(3): 880-883.

[67] Marshall L, Zukoski C F, Goodwin J W. Effects of electric fields on the rheology of non-aqueous concentrated suspensions[J]. Journal of the Chemical Society, Faraday

Just Accepted

Transactions 1: Physical Chemistry in Condensed Phases, 1989, 85(9): 2785-2795.

[68] Volkova O, Cutillas S, Bossis G. Shear banded flows and nematic-to-isotropic transition in ER and MR fluids[J]. Physical review letters, 1999, 82(1): 233.

[69] Vékás L. Ferrofluids and magnetorheological fluids[J]. Advances in science and technology, 2009, 54: 127-136.

[70] Bossis G, Lemaire E, Volkova O, et al. Yield stress in magnetorheological and electrorheological fluids: A comparison between microscopic and macroscopic structural models[J]. Journal of Rheology, 1997, 41(3): 687-704.

[71] Garnett J C M. XII. Colours in metal glasses and in metallic films[J]. Philosophical Transactions of the Royal Society of London. Series A, Containing Papers of a Mathematical or Physical Character, 1904, 203(359-371): 385-420.

[72] Rosensweig R E. On magnetorheology and electrorheology as states of unsymmetric stress[J]. Journal of Rheology, 1995, 39(1): 179-192.

[73] Klingenberg D J, Zukoski IV C F. Studies on the steady-shear behavior of electrorheological suspensions[J]. Langmuir, 1990, 6(1): 15-24.

[74] De Vicente J, Klingenberg D J, Hidalgo-Alvarez R. Magnetorheological fluids: A review[J]. Soft Matter, 2011, 7(8): 3701-3710.

Just Accepted